https://dx.doi.org/10.1016/j.jweia.2024.105695

Evaluation of active leeward side air-blowing layout on the lateral aerodynamic performance of high-speed trains in crosswinds environment: Sustainable and safe operation strategy

Zheng-Wei Chen [a, b, #], Zi-Jian Guo [a, b, #], Zheng-Xin Che [a, b], Zun-Di Huang [c, *], Yi-Qing Ni [a, b], Mei-Su Wang [a, b], Sha Huang [c], Zhi-Wei Li [c], Qian-Xuan Wang [c]

a. *Department of Civil and Environmental Engineering, The Hong Kong Polytechnic University, Hong Kong, People's Republic of China*

b. *National Rail Transit Electrification and Automation Engineering Technology Research Center (Hong Kong Branch), Hong Kong, People's Republic of China*

c. *School of Rail Transportation, Wuyi University, Jiangmen 529020, China*

[#]These authors contributed equally to this work.

*Corresponding author, email address: wyuhzd@163.com

Abstract: The lateral aerodynamic forces experienced by high-speed trains operating in crosswind environments affect trains' operating safety significantly. This paper used the Improved Detached Eddy Simulation (IDDES) method based on the Shear Stress Transport (SST) k-ω turbulence model to explore the mitigating effect of air-blowing at the leeward side of the train on the train's lateral aerodynamic forces. Different air-blowing positions and speeds were considered. The results indicate that the best mitigating effect can be achieved when simultaneously blowing air at the head, middle, and tail cars; in addition, when blowing air at the speed of 0.3 times of the resultant velocity, the rolling moment of the three cars reduced by 7.71%, 7.25%, and 25.46% respectively. Finally, the assessment of the mitigation efficiency was displayed to discuss the trade-off of rolling moment reduction and energy utilization rate for air-blowing. The research gives an insight into increasing the stability and safety of trains in crosswind based on active control, which can improve the safe operation threshold of trains.

Keywords: High-speed train; crosswind; aerodynamic lateral force; air-blowing; mitigation

1. Introduction

The wheel-rail high-speed trains, with their advantages of speed, convenience, economy, and safety, play a significant role in the sustainable development of cities (Chen et al., 2023; Liu et al., 2019; Xiong et al., 2020). However, their operating environments are becoming more complex and changeable. When the train is running on the open line, the crosswind can significantly change the lateral aerodynamic characteristics, affect the normal operation of the train, and even cause overturning (Chen et al., 2019; Guo et al., 2019, 2021). Accidents on high-speed trains caused by crosswinds occur frequently around the world (Baker et al., 2009). In response to this phenomenon, scholars have adopted the means of full-scale tests (Gallagher et al., 2018; Gao et al., 2021), wind tunnel tests (Avila-Sanchez et al., 2014; Brambilla et al., 2022; Hashmi et al., 2019; Mohebbi and Rezvani, 2021; Wang et al., 2022; Xiang et al., 2022), and numerical simulation (Liu et al., 2018; Mohebbi and Rezvani, 2019; Niu et al., 2018; Noguchi et al., 2019; Rezvani and Mohebbi, 2014), from crosswind speed (Chen et al., 2020b; Liu et al., 2020; Rong et al., 2021), yaw angle (Asress and Svorcan, 2014; Li et al., 2018; Xue et al., 2023; Zhang et al., 2018), running on bridges under crosswind conditions (Zhang et al., 2017b; Zou et al., 2020), in and out tunnels under crosswind conditions (Deng et al., 2023b; Yang et al., 2020; Zhou et al., 2021), and other aspects to analyze the impact of crosswind on high-speed trains' aerodynamic characteristics.

Scholars have adopted various methods to ensure the safety of high-speed trains operating in crosswind environments (Liu et al., 2022). During the operation of the train, the shape of the head car largely determines the magnitude of the lateral force and rolling moment on the train, optimizing the shape of the head car is an effective way to reduce the lateral load of the train (Muñoz-Paniagua and García, 2019). Chen et al. (2018) found that when the length of the nose of the train increases from 4 m to 12 m, the shedding length and influence width range of the leeward side vortex of the train decrease, and the coefficients of side force, lift force and rolling moment decrease by 10.6%, 21.7%, and 7.3%. Hemida and Krajnović (2008) examined the flow field characteristics of two train models with different lengths of the head cars under crosswind conditions. It was observed that the short-head car produced highly unsteady three-dimensional flow, which resulted in the formation of more wake vortex structures compared to the long-head car. These structures led to a surface flow that differed significantly from that observed in the case of the long-head car. Chen et al. (2020a) designed and compared the different cross-section shapes of trains, and indicated that the drum-shaped cross-section shape can reduce the

lateral force and the rolling moment by 7% and 15%.

In addition to designing the shape of the train, the windbreak wall is an effective method to reduce the lateral aerodynamic force on the train (Deng et al., 2023a; Xia et al., 2022). Tomasini et al. (2016) conducted wind tunnel tests comparing two windbreak structures. The results demonstrated that both windbreaks were effective in reducing the rolling moment coefficient by more than 30% at all yaw angles. The presence of the windbreak not only decreased the pressure on the windward side, but also altered the wake flow structure behind the train. Additionally, the analysis of the barrier coefficients revealed that the perforated sheet barrier was subjected to a wind load 20% higher than that of the band barrier at all yaw angles. Lou et al. (2022) investigated the aerodynamic characteristics of trains and bridges in the presence of crosswind and analyzed the effectiveness of curved wind barriers with different curvatures. The study revealed that wind barriers with small curvatures were effective in reducing the lateral aerodynamic force acting on trains but increased the force acting on bridges. To account for the aerodynamic characteristics of both the train and the bridge, the authors proposed the use of a curved wind barrier with a curvature of 0.35, which was found to be optimal in reducing the overall aerodynamic force acting on the system. In addition, Zhang et al. (2017a), (Mohebbi and Rezvani, 2018a; Mohebbi and Rezvani, 2018b, c), and (Mohebbi and Safaee, 2022) optimized the traditional windbreaks and achieved good mitigation effects.

Under crosswind conditions, there is a limit on the safe operating speed of trains, and when the wind speed is high enough, trains must slow down or even stop to avoid high aerodynamic forces and to ensure safety. The research on shape optimization and windbreak walls has become increasingly sophisticated and is gradually unable to meet the train's speed-up requirements in more complex running conditions, new mitigating methods are thus needed to explore. Flow field active control technology has made significant progress in the field of aviation and aerospace and has been proven to improve flow field structures and reduce object aerodynamic forces (Tardu and Doche, 2009; Wahidi and Bridges, 2012). In the high-speed train field, Chen et al. (2022) studied the effect of air-blowing on the lateral aerodynamic force experienced by trains and achieved a reduction in the lateral rolling moment of 18.5% for the head car, 21.7% for the middle car, and 30.8% for the tail car. This study demonstrates that air-blowing can reduce the lateral wind aerodynamic force on trains, but the blowing effect from each car and different blowing speeds are not studied.

In this paper, the mitigation effect of the air-blowing positions at different cars and

blowing speeds on the lateral aerodynamic forces and the characteristics of the flow field of the train in a crosswind environment are investigated. The structure of the paper is as follows: the introduction of the high-speed train model, computational domain, grid scheme, solution method, and validations are included in Section 2; the results analysis of air-blowing positions and speeds, and the mitigation efficiency assessment are included in Section 3; the conclusion and summary are included in Section 4.

2. Computational model and methodology

2.1. Geometry model and computational domain

This paper conducts numerical simulation research based on the CRH380A high-speed train model. The train model contains three cars, which are the head, middle, and tail cars. Small structures such as headlights and door handles were removed and retained the main geometric features such as train bogies and inter-carriage structures. As shown in Fig 1(a), define the top surface of the rail as the reference plane (Z = 0), and the center of the rail as the reference line (Y = 0). The height of the train is h = 3.7 m, the width of the train is 3.38 m, and the height of the track subgrade is 1 m. The middle height position of the train is defined as MOT. It can be seen from Fig. 1(b) that the length of the head and tail cars are both 26.5 m, and that of the middle car is 25 m, the total length of the train is L = 78 m. In this paper, four cases, the original train (Ori), blowing air at the head car only (H), blowing air at the head and tail cars (HT), and blowing air at all three cars (HMT) are studied. The air-blowing slots of the head car and the tail car are both 10.2 m in length, and that of the middle car is 7.14 m. Combined with Figs. 1(c)-(e), it can be seen that the widths of the three air-blowing slots are 0.1 m, the interval between each slot is 0.37 m, and the vertical position is 0.2 m above the MOT. To avoid affecting the cab windows of the head car and the tail car, the length of three air-blowing slots changed gradually for the head car and tail car.

To better align with the requirement of the utilized turbulence model, the computational domain was scaled down by 1/8, and the train height $h \approx 0.463$ m as the characteristic length of the flow field after scaling. The size of the computational domain is shown in Fig. 2, the distances from the front and the side inlets to the train are 25 h and 12 h respectively to ensure the stability of the incoming flow; the distances from the rear and the side outlets to the train are 45 h and 25 h respectively to ensure the full development of the flow field around the train, and avoid the influences of the boundaries on the flow field around the train, which is also the main reason why the height of the calculation

domain is 18 h.

Both inlets were set as the velocity inlet boundary with the velocity vector of V_x = 55.56 m/s, V_y = 25 m/s, V_z = 0 m/s, the resultant velocity $U_s \approx$ 60.92 m/s, the Reynolds number is equal to 1.9 × 10^6, the yaw angle is 24.24°; the outlets were both set to zero pressure outlet; the ground containing the track was set as moving no-slip wall, and moves with a velocity vector of V_x = 55.56 m/s, V_y = 0 m/s, V_z = 0 m/s, to simulate the relative motion between the train, the track and the ground; the top surface was set as a symmetrical wall. Note that the boundary conditions of all air-blowing slots are set as velocity inlet boundary conditions.

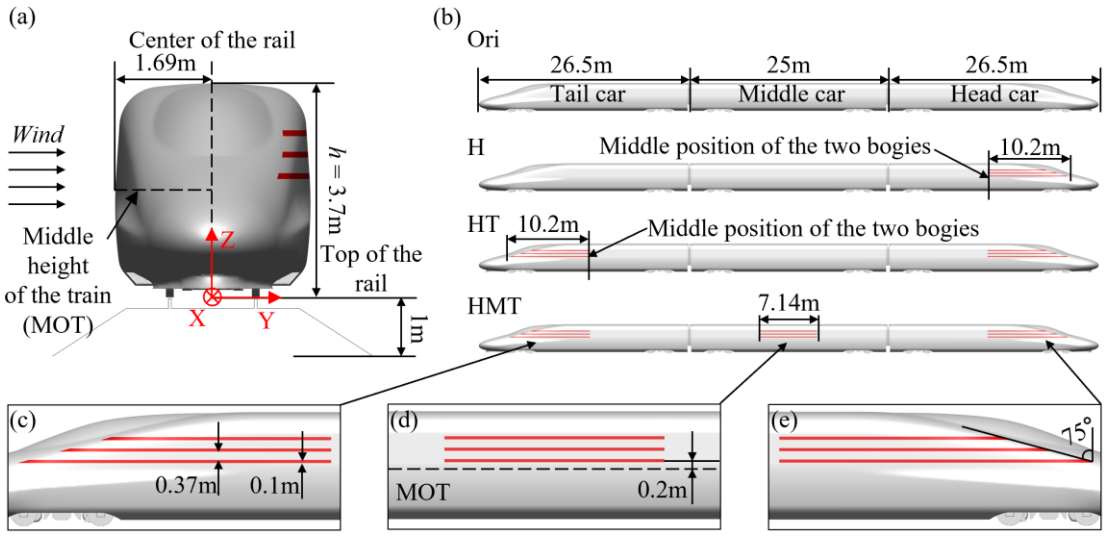

Fig. 1. The details of the high-speed train model.

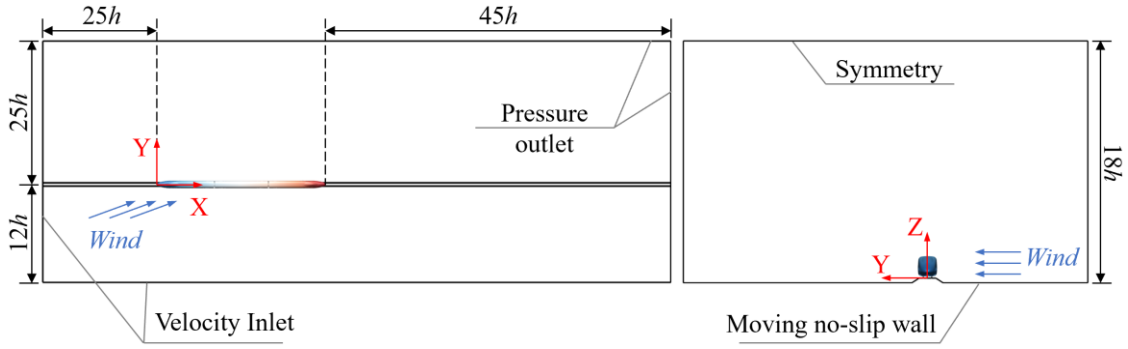

Fig. 2. The details of the calculation domain.

2.2. Meshing strategy

The computational domain was discretized into three parts by using the trimmed meshing method, including the prism layer grid near the surface of the train, the refined zones, and the core zone, as shown in Fig. 3. The total thickness of the prism layer grid in this study is 0.016 h, and there are 12 layers in total, the thickness difference of each layer

is 1.2 times, and the average y^+ is about 7.6. For all Fluent models based on the ω-equation, the y^+-insensitive wall treatment has been defined to ensure the attainment of accurate flow structures in the vicinity of the wall. (Chen et al., 2022). Under crosswind conditions, the flow fields of the leeward side of the train and the wake area are complex and wide-ranging, therefore, the grids in these areas were refined to obtain accurate flow information. Referring to the grid refinement method of (Muld et al., 2012), the refined zones were divided into three parts, and the grid sizes are 0.022 h, 0.044 h, and 0.088 h respectively. The refined zones and the prism layer are shown in Figs. 3(d)-(g).

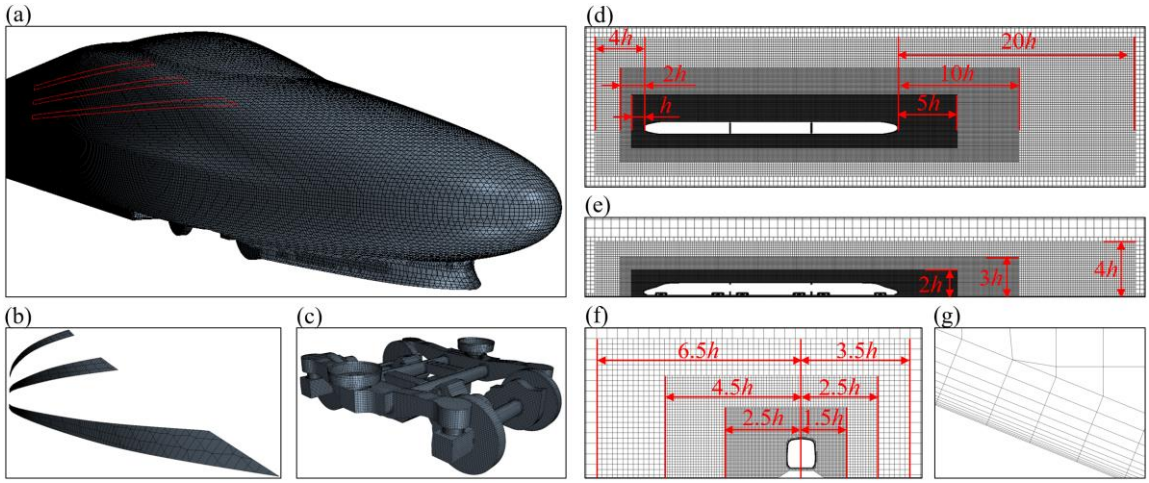

Fig. 3. Grids of (a) train surface, (b) air-blowing slots on the head car, (c) bogie, (d) top-view of the refined zone, (e) side-view of the refined zone, (f) front-view of the refined zone, and (g) prism layer.

To eliminate the influence of grid size on calculation results and save computing resources, three meshing schemes were carried out in this paper. The grids of the prism layer and the refined zones of the three schemes are consistent, and the grid size of the train surface was changed to test the grid independence. The minimum grid sizes on the train surface of the three schemes are 0.022 h (coarse), 0.011 h (medium), and 0.005 h (fine) respectively, and the total grids are 14.7 million, 29.8 million, and 54.2 million, respectively.

By comparing the pressure coefficient C_p, which is defined as Formula (1), on the Y = 0 section of the case of Ori, as Fig. 4(a) shows, it can be seen that although C_p of the Coarse case is consistent with Medium and Fine case in the variation trend, there are obvious differences in value, while there is no significant difference between Medium and Fine; observing the lateral force coefficient C_y, which is defined as Formula (2), calculated by the three schemes in Fig. 4(b), it can be found that the C_y of the head and tail cars of Coarse are significantly less than that of Medium and Fine; although the C_y of the head and tail cars of Fine is slightly larger than that of Medium, the overall difference is less than 1%. In summary, the Medium grid can achieve the calculation accuracy of Fine. Therefore,

the Medium meshing scheme is selected as the scheme of all the cases in this research. The grid of the train surface, the air-blowing slots, and the bogie are shown in Figs. 3(a), (b), and (c), respectively.

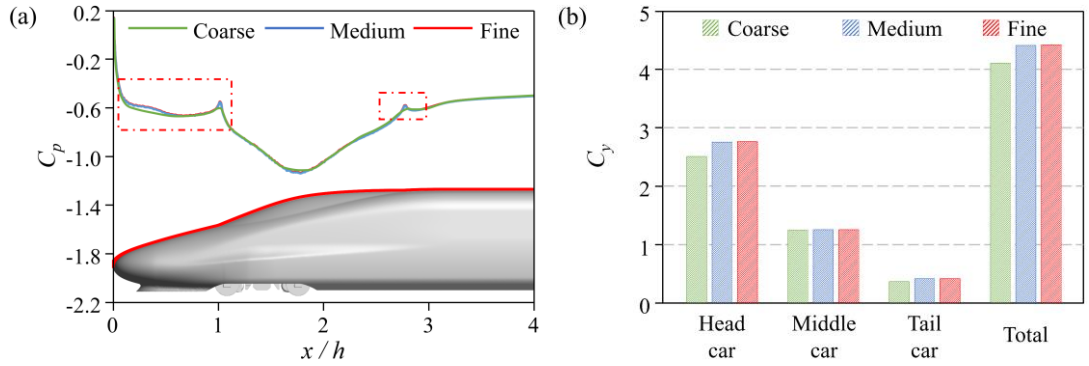

Fig. 4. The comparison of the three meshing schemes of (a) C_p of Y = 0 curve of the train's top surface and (b) C_y of the three cars and total.

2.3. Numerical solution scheme and verification

In this paper, the IDDES method based on the incompressible SST k-ω turbulence model, which has been widely used in high-speed train fields (Che et al., 2023; Huang et al., 2016), was used to simulate the flow field characteristics of the train running under the crosswind condition. The pressure-velocity coupling scheme was Semi-Implicit Method for Pressure Linked Equations-Consistent (SIMPLEC), the least squares cell-based method was used to calculate the gradient in the discrete term, and the pressure term was set to the second order. The time step Δt was set to 8×10^{-5} s to maintain the Courant number $CFL \approx 1$ ($CFL = U\Delta t/\Delta x$, directly proportional to the incoming flow velocity U and time step Δt, and inversely proportional to the streamwise size of the cell). Also, 10000 steps of transient calculation and 10000 steps of time-averaged processing were processed to ensure the full development of the flow field and guarantee enough transient data to get time-averaged physical quantities such as the velocity, pressure, and vorticity information. Each calculation step iterates 30 times, and the residual was 10^{-5}.

The data from the wind tunnel test of (Niu et al., 2016) was used to verify the feasibility of the numerical solution scheme above. The test was conducted in the high-speed test section of the wind tunnel in central south university (CSU). The cross-sectional area and the length of the test section is 3×3 m^2 and15 m, respectively. A working condition with an incoming velocity of 60 m/s, a yaw angle of 15°, and a turbulence intensity of less than 0.5% is used to validate the present numerical method. As shown in Fig. 5, A two-car formation train with a scale of 1:8 is used as the test model, with a characteristic height

same as the numerical simulation. The Reynolds number obtained based on the above parameters is 1.9×10^6. For more details on the experiment please refer to Niu et al., (2016).

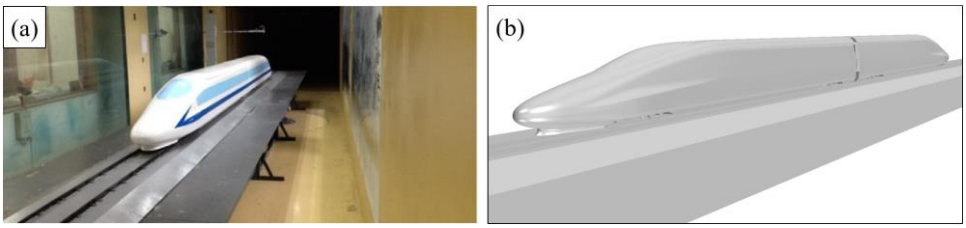

Fig. 5. The train models of (a) wind tunnel test and (b) numerical simulation.

The side force coefficient C_y and the lift force coefficient C_z, which are defined as Formula (2) and (3), of the head car and the tail of the wind tunnel test and the simulation are presented in Table 1, it can be found that the absolute values of the differences of C_y and C_z between the two cases are all below 10%. In addition, according to C_p of the Y = 0 curve of the head and tail cars' top surface of the two cases in Fig. 6, it can be demonstrated that the C_p of the two cases matches well. To sum up, the numerical solution scheme of this paper is feasible and reliable.

Table 1. Differences of the C_y and C_z between the simulation and the tunnel test

	Head car		Tail car	
	C_y	C_z	C_y	C_z
Wind tunnel test (Niu et al., 2016)	1.677	1.594	0.237	1.029
Numerical simulation	1.622	1.526	0.248	1.096
Absolute difference	3.28%	4.27%	4.64%	5.54%

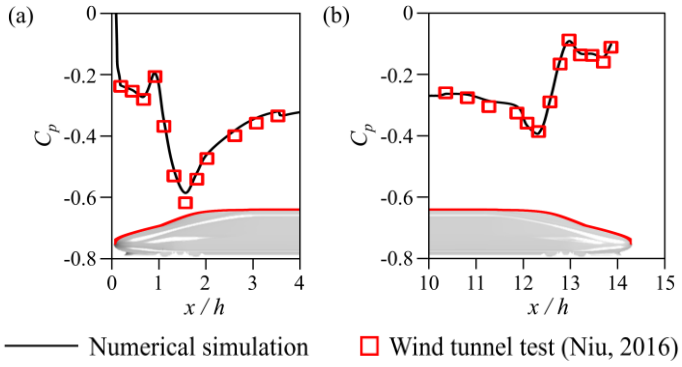

Fig. 6. The C_p of Y = 0 curve of the train's top surface of the wind tunnel test and the simulation of (a) the head car and (b) the tail car.

3. Results and analysis

As shown in Fig. 7(a), the longitudinal middle positions of the air-blowing slots at the leeward side (*LWS*) of the head car, the middle car, and the tail car are marked as *X*1, *X*2,

and $X3$, and the middle position between the bottom and the middle air-blowing slots is marked as $Z1$. Mark the train surface above the air-blowing slots as *SAA*, the surface between the slots as *SBA*, and the surface under the slots as *SUA* to accurately analyze the influence of air-blowing on the surface pressure around the blowing slots, as shown in Fig. 7(b).

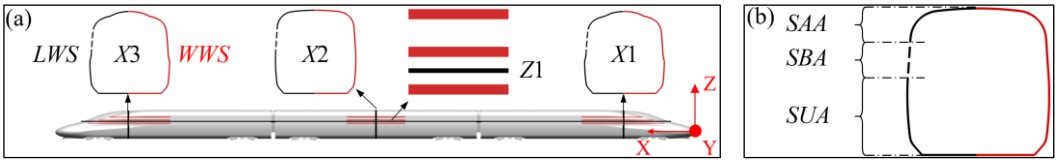

Fig. 7. The details of (a) the positions of $X1$, $X2$, $X3$, and $Z1$ and (b) the ranges of *SAA*, *SBA,* and *SUA*.

In addition, the dimensionless coefficients of the lateral force (C_y), lift force (C_z), rolling moment (C_{mx}), and their respective reduction rate ζ_i are defined below:

$$C_p = \frac{P - P_0}{0.5\rho U_s^2} \tag{1}$$

$$C_y = \frac{F_y}{0.5\rho U_s^2 A} \tag{2}$$

$$C_z = \frac{F_z}{0.5\rho U_s^2 A} \tag{3}$$

$$C_{mx} = \frac{M_x}{0.5\rho U_s^2 A l} \tag{4}$$

$$\zeta_i = \frac{C_i - C_{i0}}{C_{i0}} \tag{5}$$

where the pressure distribution P, the lateral force F_y, the lift force F_z, and the rolling moment M_x are calculated by Fluent; ρ = 1.225 kg/m^3 stands for the air density; The reference area A pertains to the projected cross-sectional area of the full-scale train model and measures 11.22 m^2. The reference length, represented by l, is set at a value of 3 meters for full-scale size. The i in Formula (5) represents y, z, and mx. The C_y, C_z, and C_{mx} decrease when ζ_i is negative.

3.1. Influence of air-blowing position on the train aerodynamic loads and the flow field

Fig. 8 shows the ζ_y, ζ_z, and ζ_{mx} obtained when blowing at $0.1U_s$ at different positions. Under crosswind conditions, the C_y and C_{mx} are usually used as important parameters for the estimate of train operation safety, and the C_{mx} is mainly affected by the C_y (Xia et al., 2022). Based on the observations made in the study, it was found that C_y of the head car decrease by 2.06%, while that of the middle and tail cars increase when considering H. In the case of HT, C_y of the head car decrease, and the tail car was optimized, ζ_y of the tail car is -15.68%, the C_y of the middle car, however, is still increasing; when also blowing at

the middle car (HMT), the values of C_y of the three cars are reduced by 2.12%, 4.44%, and 20.97% respectively. Although the C_z of the tail car increased by 0.75% in HMT, the C_{mx} of the three cars decreased, according to the ζ_{mx}, by -6.21%, -4.75% and -19.67% respectively. Overall, when blowing at all three cars at the same time (HTM), the lateral characteristics of the whole train have achieved the best migrating results.

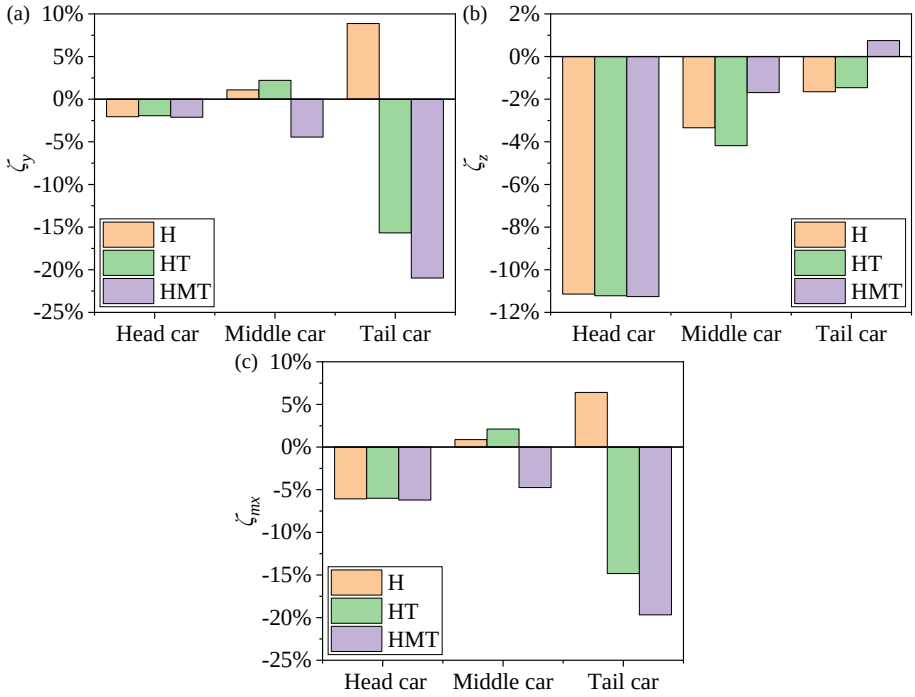

Fig. 8. The reduction rate ζ_i of the three cars of H, HT, and HMT. The reduction rates are (a) reduction rate of lateral force ζ_y, (b) reduction rate of lift force ζ_z, and (c) reduction rate of rolling moment ζ_{mx}.

Air-blowing inevitably affects the flow field structure around the train and the surface pressure of the train. Figs. 9(a)-(c), and Figs. 9(d)-(e) shows the windward side (*WWS*) and leeward side (*LWS*) train surface pressure coefficient C_p curves at locations of $X1$, $X2$, and $X3$, respectively. The green rectangles in Fig. 9 are the positions of the blowing slots. The C_p of the *LWS* of the train at the three locations is negative. Observing the curves of H in Figs. 9(a)-(c), for the head car, although the negative pressure C_p of *SUA* is increased by air-blowing, that of the *SBA* and *SAA* decreases; C_p of the middle car slightly changes; for the tail car, C_p of *SUA* increases, but there is no obvious change in that of *SAA*, which is the main reason for the increase in C_y of the tail car. According to the HT curve, the C_p of *SUA* is reduced while blowing air at the tail car, but that of *SAA* slightly increases. In accordance with the curves of HMT, air-blowing at the middle car reduces the C_p of *SUA*. According to Fig. 9(d)-(e), blowing air at the *LWS* has no obvious influence on the pressure on the *WWS* surface of the train.

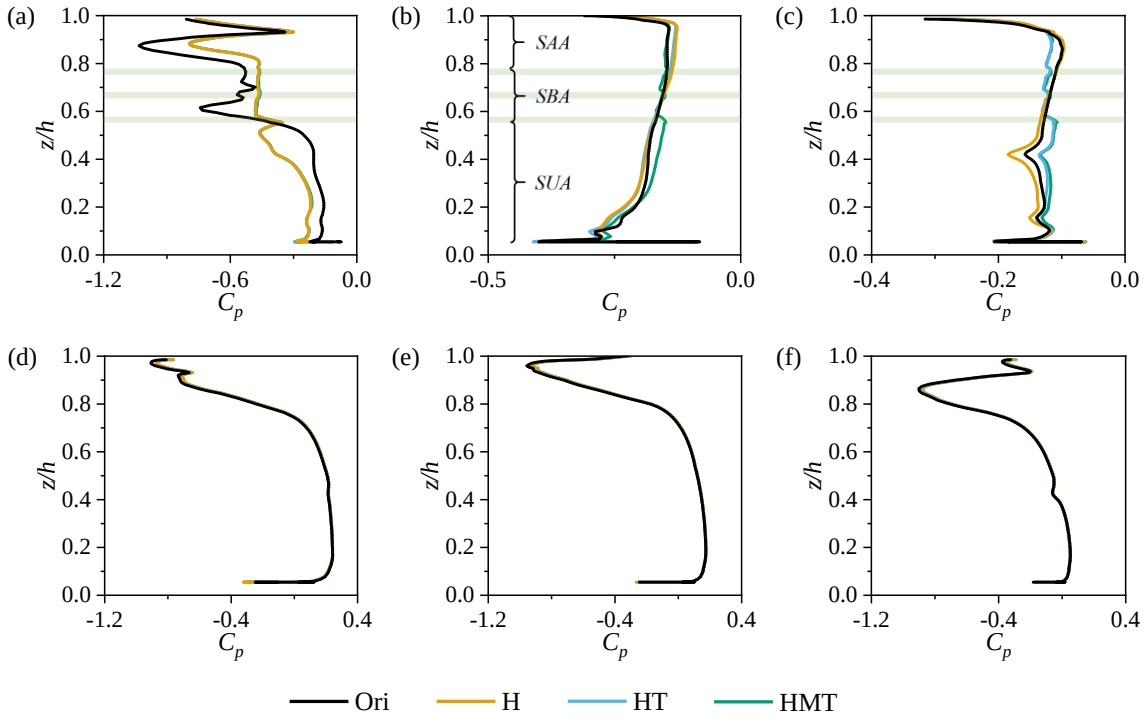

Fig. 9. The c_p of the train surface (green rectangles are the locations and of the three slots) at different positions of (a)-(c) *LWS* of *X*1-*X*3 positions, and (d)-(e) *WWS* of *X*1-*X*3 positions.

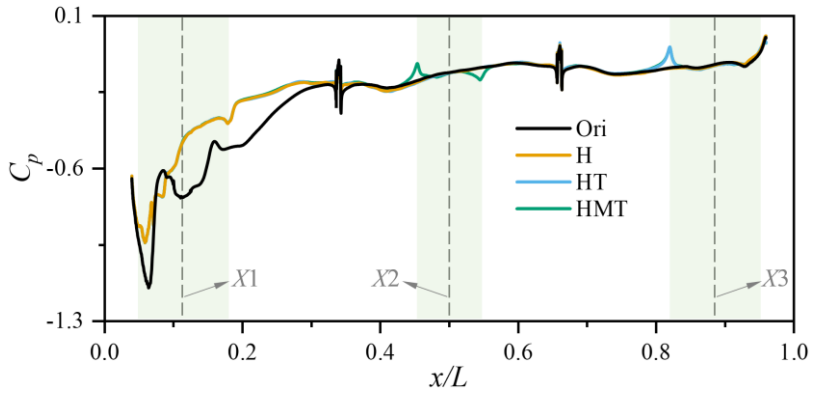

Fig. 10. The C_p of *Z*1 while air-blowing at different positions.

Combining the C_p of *Z*1 in Fig. 10 and the pressure distribution of the *LWS* of the train in Fig. 11, blowing air at the head car disturbs the distribution of negative pressure on the train surface. There are mainly two negative pressure zones (*MPZ*-1 and *MPZ*-2) on the *LWS* of the head car, as shown in Ori in Fig. 11. *MPZ*-1 disappears caused by air-blowing, along with the range and negative pressure value of *MPZ*-2 significantly reduced. The negative pressure value behind the air-blowing slots of the head car was also reduced, as shown in Fig. 10. Although the negative pressure of the *SUA* increases (Fig. 9(a)), the C_y and C_z of the head car decreased. It can be demonstrated from the pressure curve of the middle car that blowing air causes the pressure on both sides of the slots to change in the opposite direction, and the change amplitude is relatively close. Although smaller the

surface pressure of the middle car is, and the pressure distribution has no obvious change, the negative pressure of the *SUA* of the middle car has decreased as shown in Fig. 9(b). Blowing air at the tail car reduces the negative pressure on the front surface of the slots, which means that the C_y decreases.

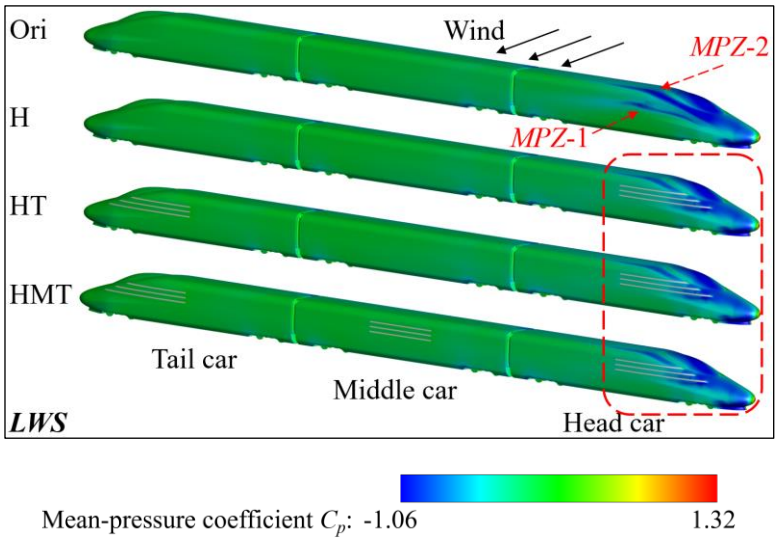

Fig. 11. The pressure distribution of the *LWS* surface of the four cases.

To further analyze the impact of air-blowing on the *LWS* flow field, the instant Q criterion vortex structure diagram and time-average 3-D streamlines are given in Figs. 12(a) and (b). The Q criterion diagram clearly shows the influence of air-blowing at the head car on the vortex, and the black dotted lines represent the slots' positions. Observing the vortex structure of Ori, the overall vortex structure on the *LWS* is similar to Chen et al. (2019). On the *LWS* of the streamlined surface of the head car, a vortex attached to the train surface is formed, which detaches from the cross-sectional sections of the head car to form the main vortex structure V1 on the *LWS*. By comparison, with air-blowing, the position of V1's formation and detachment are delayed, generally at the edge of the blowing slots, and the vortex originally attached to the streamlined head surface disappeared, which further explains the reason for the disappearance of *MPZ*-1 in Fig. 11. Fig. 12 (c) visualizes the localized flow near the air-blowing slot using the lateral component of the velocity on X1 slice to explore how the blowdown affects the formation of V1. According to Fig. 12 (c), the air-blowing re weakens the reverse lateral velocity near the upper leeward side of the head car, creating a larger region of near-0 velocity, which prevents the formation of V1 at what a higher and closer location to the leeward side would otherwise be. In addition, by comparing H, HT, and HMT, blowing at the tail car has an interfering effect of the stability on the vortex V2 in wake area. The 3-D streamlines reflect the airflow trajectory. The blowing positions are indicated as *BA*. By comparing Ori and H, the airflow near the head

car is farther from the surface when blowing at the head car. Compared to Ori, the leeward vortex streamlines are more dispersed after blowing, reflected in the figure as *D* being larger, which is due to the reduction of the verticity of V1 caused by blowing. By comparing H, HT, and HMT, the leeward flow structures are similar, especially *d* are consistent, further confirming that blowing air at the head car has the greatest impact on V1 while blowing at the middle and the tail cars have no obvious impact on the leeward vortex.

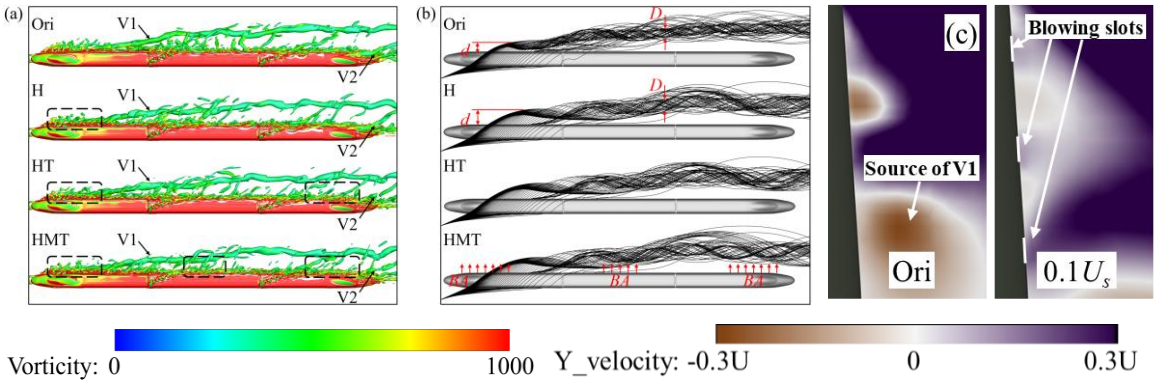

Fig. 12. Flow structure in the forms of (a) Q criterion (Q = 30000), (b) 3-D streamline, and (c) lateral component of the velocity

Fig. 13 shows the Z-Y cross-sectional vorticity of *X*1, *X*2, and *X*3 positions of air-blowing at different positions. By comparing *X*1, the vorticity around the blowing position (it is indicated by *BA*) of the head cars is larger with air-blowing, with an angle obliquely downward, which is due to the large air velocity at the top of the head rotating with the blowing air. For *X*2 position, compared to Ori, although the vorticity of the vortex is smaller, blowing at the head car has caused the *LWS* vortex core (it is indicated by *EC*) of V1 to be closer to the train surface, reflected in Fig .13 is that the distance between V1 and the train surface (*Dvt*) became smaller, and further away from the ground (*Dvg* is larger). Differed from H and HT, HMT has increased air rotation near the blowing slot of the middle car blowing, with an obliquely upward direction, which is due to the upward movement of the air from the bottom of the train and the interaction of the air blown from the slots. Furthermore, by comparing the *EC* of H, HT, and HMT, blowing at the middle car only affects the flow field structure near the blowing slots and has no obvious impact on V1. In accordance with the vorticity of *X*3, it can be concluded that V1 of H, HT, and HMT are the same, and the vorticity of the vortex relative to Ori and the *Dvt* is smaller. For HT and HMT with blowing air at the tail car, the vorticity of the air near the blowing slots increases, changing the airflow near the blowing slots, however, this phenomenon is local, and blowing air at the tail car has no obvious impact on V1.

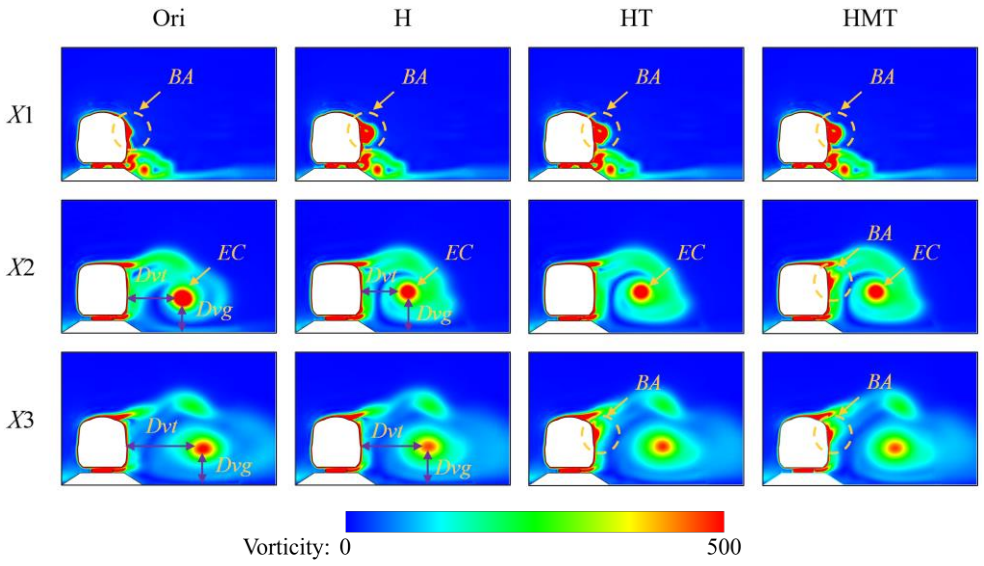

Fig. 13. The vorticity of $X1$, $X2$, and $X3$ slices of air-blowing at different positions.

The effect of air-blowing on the airflow around the slots can be clearly displayed in the streamlines diagram in Fig. 14. Observing the position of $X1$, the two vortices that originally close to the train surface were disappeared, while a new large vortex and a small vortex close to the surface appeared when blowing air at the head car. According to the $X2$ position of HMT, due to the upward movement of the air under the train and the interaction with the blown air, small vortices are formed on the surface above the blowing slots; blowing air at the tail forms a small vortex above the slots. The small vortices around the slots are the important reasons for the change in the surface pressure of the train.

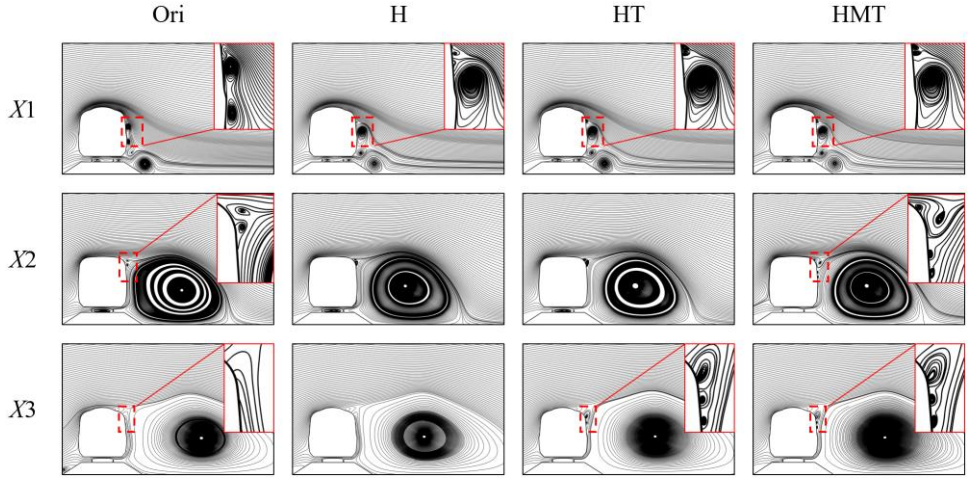

Fig. 14. The 2-D streamlines of $X1$, $X2$, and $X3$ positions of air-blowing at different positions.

3.2. Influence of air-blowing speed on the train aerodynamic loads and the flow field

Based on the conclusions of section 3.1, the mitigating result on the crosswind characteristics of the train obtained by blowing air at all three cars at the same time (HMT) is relatively the best, but the blowing speed (V_b) also has a significant impact on the flow

field structure on the *LWS*. Therefore, this section studies the crosswind characteristics of the train when blowing air at different speeds in the case of HTM. The blowing speeds are from $0.05U_s$ to $0.3U_s$, with $0.05U_s$ as the speed interval.

Fig .15 shows the ζ_y, ζ_z, and ζ_{mx} obtained by blowing air at different speeds in the case of HTM. From the analysis of ζ_y, it can be demonstrated that blowing air at all V_b decreases the C_y of the three cars. For the head car, the mitigating result on the C_y increases with the increase of V_b. When $V_b = 0.3U_s$, ζ_y of the head car is -3.33%. For the middle and tail cars, blowing air can also reduce their C_y. Due to the small value of the aerodynamic force of the tail car, little changes cause large fluctuations in the value. When $V_b = 0.3U_s$, the lateral force of the middle car and the tail car decreases by 7.72% and 29.4% respectively. The C_z of the head car decreases with the increasing V_b. However, when V_b is larger than $0.2U_s$, the C_z of the middle car shows a negative growth trend. Under the combined effect of C_y and C_z, air-blowing at different speeds reduce the C_{mx} of the three cars, and the ζ_{mx} of the head car shows an increasing trend with the increase of air-blowing speed. When $V_b = 0.3U_s$, the ζ_{mx} of the three cars are -7.71%, -7.25%, and -25.46% respectively.

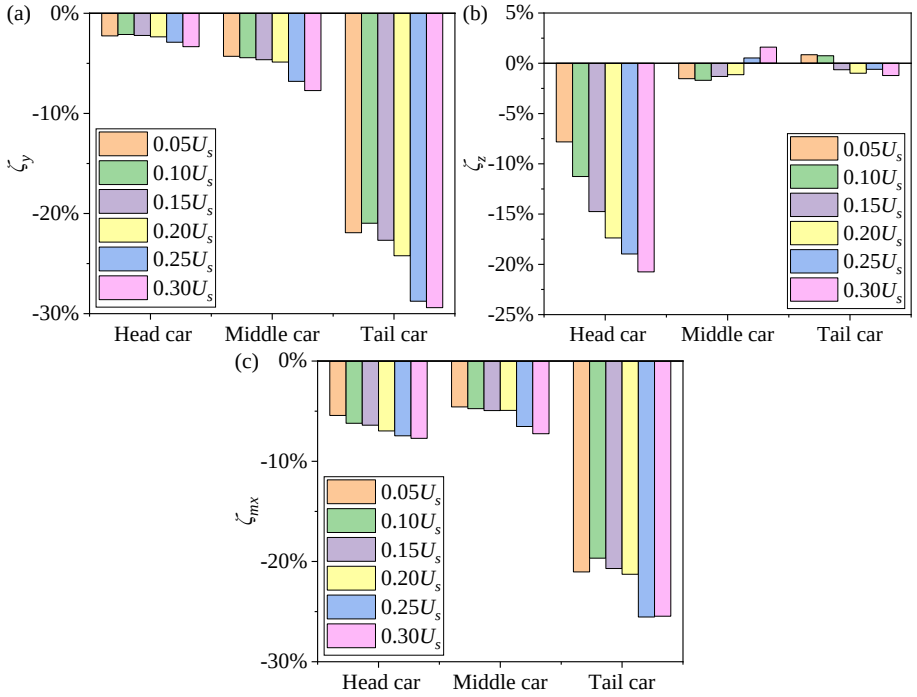

Fig. 15. The reduction rate ζ_i of the three cars of different V_b. The reduction rates are (a) reduction rate of lateral force ζ_y, (b) reduction rate of lift force ζ_z, and (c) reduction rate of rolling moment ζ_{mx}.

Figs. 16 (a)-(c), and (d)-(e) show the *LWS* and *WWS* train surface pressure coefficient C_p curves at $X1$, $X2$, and $X3$ respectively when blowing air at different V_b in the case of HMT. It can be represented from Fig. 16(a) that blowing air at the head car makes the C_p of *SUA* negatively increase, while that of *SBA* and *SAA* decreases, and the degree of changes

is positively correlated with V_b. Furthermore, it was observed that the negative pressure at the bottom of the train increased, which directly contributed to the decrease in C_z of the head car. The surface pressure distribution on the *LWS* of both the middle and tail cars exhibited similar changes with respect to V_b, as illustrated in Figs. 16(b)-(c). which is the C_p of *SUA* decreases and that of *SBA* and *SAA* increases. The degree of change increases with the increase of V_b. According to Figs. 16(d)-(e), the results indicates that the application of blowing air on the *LWS* of the train has negligible impact on the pressure distribution on the *WWS* surface of the train.

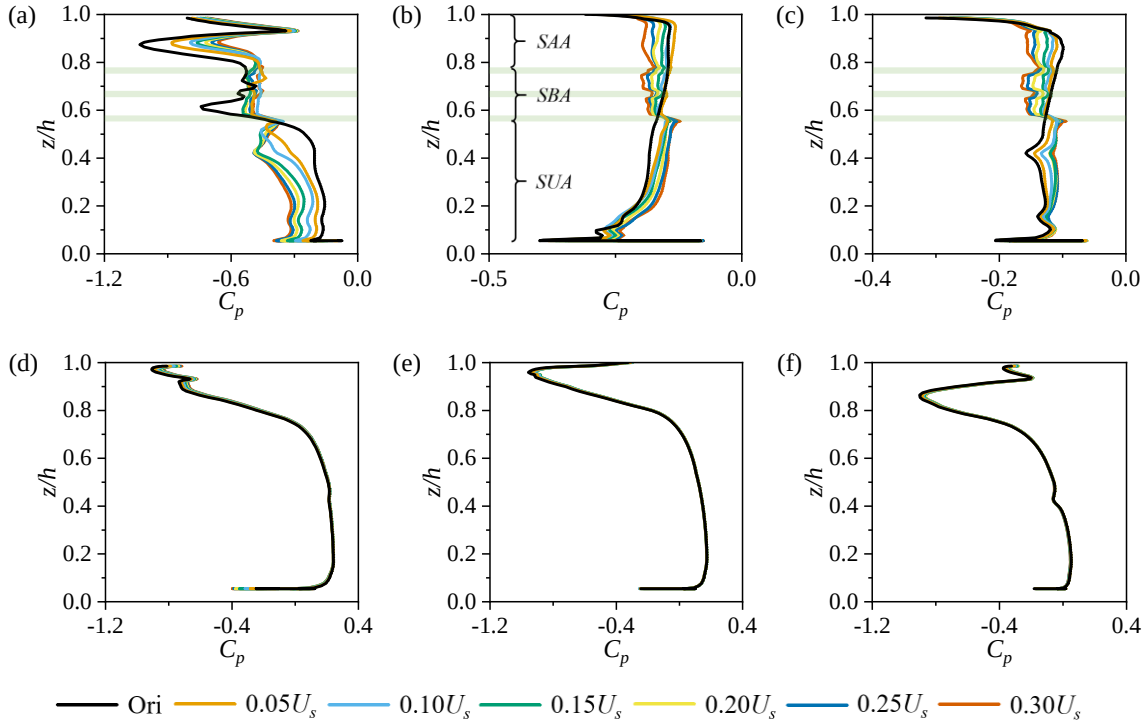

Fig. 16. The C_p of the train surface of different V_b (green rectangles are the locations and the ranges of the three slots) at different positions of (a)-(c) *LWS* of *X*1-*X*3 positions, and (d)-(e) *WWS* of *X*1-*X*3 positions.

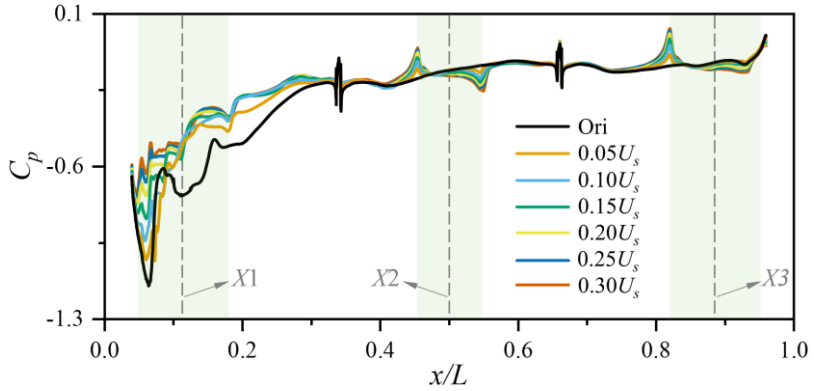

Fig. 17. The C_p of *Z*1 while air-blowing at different V_b.

Combining the pressure distribution of the *LWS* of the train in Fig. 18 and the C_p of

$Z1$ in Fig. 17, the Ori and $0.1U_s$ show that blowing air at the head car makes the negative pressure zone *MPZ*-1 disappear, and the negative pressure value and range of the *MPZ*-2 decrease. With the increase of V_b, the negative pressure zone of the streamlined part of the head car significantly faded. Combined with the pressure curve of $Z1$, blowing air at the head car makes the C_p near the slots rise, and the degree of rise is gradually obvious with the increase of V_b. The C_p behind the slots of the head car also reduces, but the degrees of reductions are familiar when V_b is greater than $0.1U_s$. The surface pressure changes at both ends of the slots of the middle car are obvious, the front end rises and the rear end falls. The change degree is similar and gradually increases with the increase of V_b. The surface pressure at the front end of the slots of the tail car rises, and as V_b increases, the C_p between the slots begins to decrease, this phenomenon became more obvious with the increasing V_b.

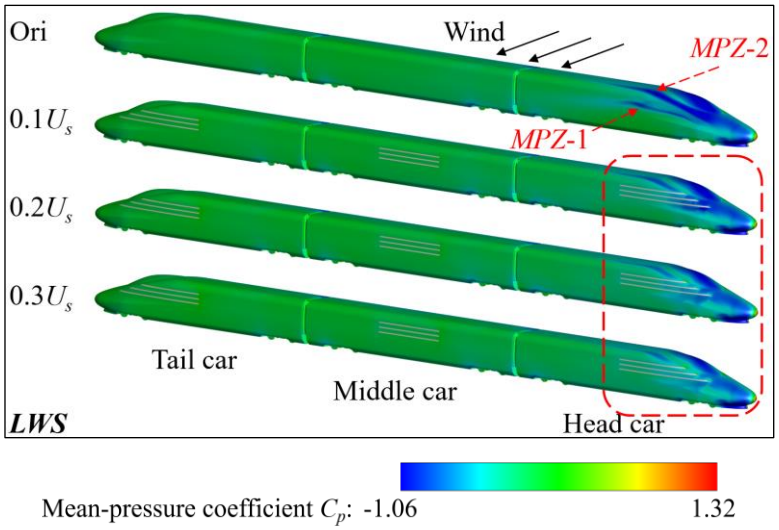

Fig. 18. The pressure distribution of the *LWS* surface of the train when blowing at different V_b.

Figs. 19(a) and (b) show the instantaneous Q-criteria vortex structure diagram and time-average 3-D streamline diagram. It can be concluded from the Q criterion diagram that as V_b increases, the vortex structure near the slots of the head car becomes more complex, and the number of small vortices gradually increases. This shows that the greater the V_b, the stronger the level of air-blowing interference to the surrounding flow field structure. The vortex V1 on the *LWS* of the train and the vortex V2 at the wake of the train are greatly affected by V_b. In the case of the same Q value, when the V_b is $0.3U_s$, the spatial structure of V1 is no longer continuous, while V2 was already incomplete when $V_b = 0.2U_s$. Observing the spatial position of V1, it can be seen that the impact of the air-blowing speed on the spatial position of V1 is mainly reflected in the vicinity of the slots of the head car. A larger blowing speed will make V1 farther away from the train, which causes the spatial position of V1 on the *LWS* of the middle and tail cars gradually move away from the surface.

In the current range of V_b, blowing air at the middle car and the tail car still has no obvious impact on the spatial structure and position of V1, which is also reflected in the analysis of vorticity. Comparing d in the streamline diagram, blowing air at the head of the train blows the air away from the surface of the train, and as V_b increases, the greater d is, and the greater the impact of air-blowing on the flow field on the *LWS* of the head car. Air-blowing interferes with the generation and shedding of the *LWS* vortex at the head car. Although it fails to completely hinder the formation of the vortex, it reduces the vorticity of the vortex, which is reflected in the streamline diagram, that is, D is larger, and this phenomenon becomes more obvious as the blowing speed increases. The blowing velocity does not contribute to the formation mechanism of V1, but it is the root cause of the outward and downward shift of the vortex core of V1, which corresponds to the increase of d and D in Fig. 19(b).

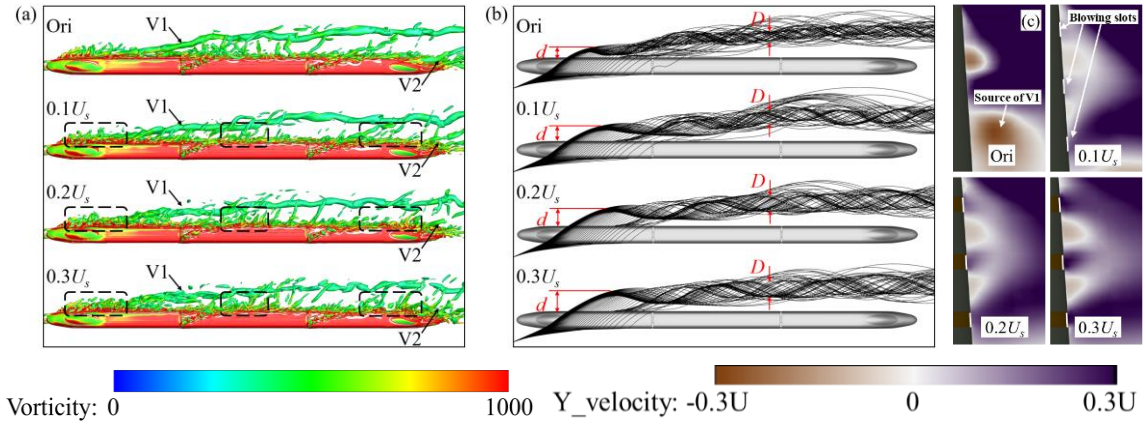

Fig. 19. Flow structure in the forms of (a) Q criterion (Q = 30000), (b) 3-D streamline, and (c) lateral component of the velocity

Fig. 20 shows the Z-Y cross-section vorticity of $X1$, $X2$, and $X3$ positions when blowing at different speeds in the case of HTM. For $X1$ position, the air-blowing increases the vorticity near the slots. With the increase of the air-blowing speed, the range of the large vorticity area increases and gradually moves away from the train surface in an oblique downward. It can be seen from the vorticity diagram at $X2$ that compared with Ori, the vorticity of *EC* beside the head car is reduced by air-blowing, and the degree of reduction increases with the increase of V_b. The *Dvt* gradually increases, and *Dvg* is almost the same. In addition, the vorticity near the slots increases, and the direction is oblique upward. With the increase of V_b, the range of air-blowing influence gradually increases, but its influence range is still near the train surface, and the impact on V1 on the *LWS* is still not obvious. According to the position of $X3$, the vorticity of V1 after air-blowing is less than Ori, and the larger the V_b, the smaller the vorticity. Compared with Ori, the position of *EC* is still

closer to the train surface, but its impact on the surface pressure of the train is not significant. By observing the vorticity near *BA*, it can be seen that the air below the train interacts with the air blown out by the slots, which increases the air curl and inclines upward, which is the main reason for the pressure change on the train surface.

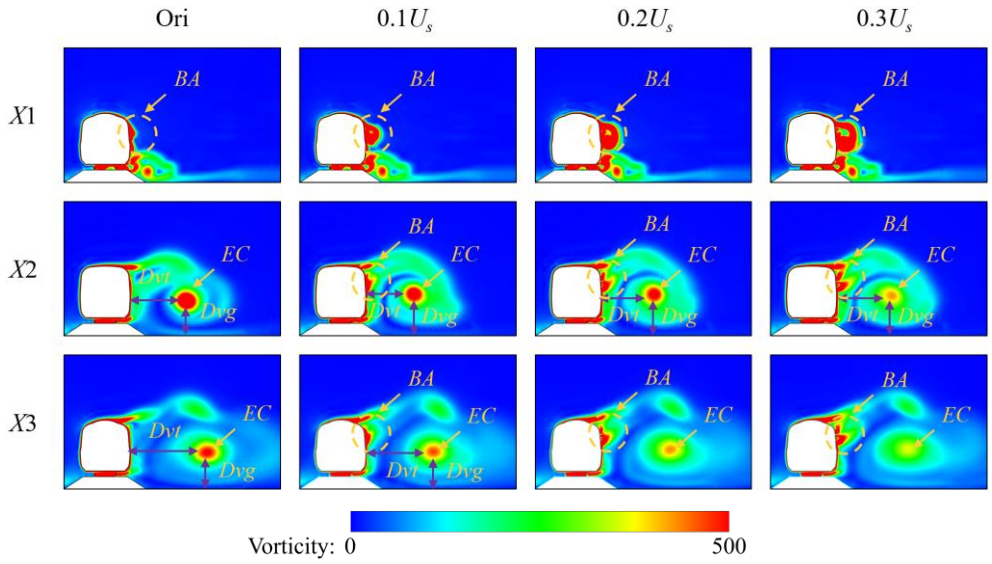

Fig. 20. The Z-Y cross-sectional vorticity of *X*1, *X*2, and *X*3 positions of air-blowing at different V_b.

Based on the Z-Y streamline diagram in Fig. 21, the flow field changes can be further observed. With the increase in V_b, the interference intensity of air-blowing on the flow field gradually increases. Comparing the flow fields of $0.1U_s$ and $0.3U_s$, it can be demonstrated that the larger the V_b, the larger the size of the vortex, which is gradually away from the train surface. The air blown out from the slots at the middle car and the tail car coupled with the incoming flow under the car body produces small vortices. With the increase of V_b, the size of the small vortices increases, and also shows a trend of being far away from the train surface.

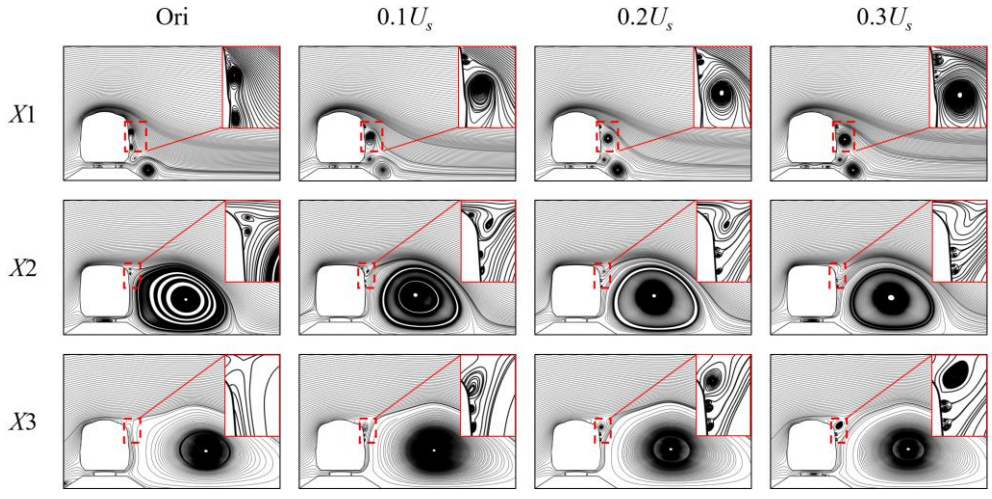

Fig. 21. The 2-D stream trace of *X*1, *X*2, and *X*3 positions of air-blowing at different V_b.

3.3. Mitigation efficiency assessment

Safety is the main consideration factor for trains operating in crosswind conditions, The reduction of the lateral force and overturning moment can bring positive feedback to the safety of the train. More directly, it will reduce the overturning coefficient and derailment coefficient of the train in the crosswind environment, which are two direct indicators to evaluate the safety of trains in vehicle system dynamics, therefore improve the safety threshold of trains operating in crosswind environment. As analyzed above, simultaneously blowing air at the head car, the middle car, and the tail cars can reduce the lateral force and rolling moment of the train, improving its safety in crosswind environments. This phenomenon becomes more apparent as the blowing speed increases. Further increasing the V_b can further reduce the rolling moment, but the necessity of further increasing the V_b needs to be discussed. In response to this issue, this section references (Xu et al., 2022) and analyzes the mitigating benefit of the lateral aerodynamic forces experienced by the train obtained at different blowing speeds, using the rolling moment M_x as a standard and evaluating the necessity of further increasing the blowing speed from the perspective of energy utilization rate.

According to the literature, C_E is used to evaluate the energy consumption generated by air-blowing, which is defined as Formula (6). The reduction of the rolling moment brought by air-blowing is represented by ΔM_x, which is composed of the force F_{mx} and the moment arm. Taking h as the moment arm, then $F_{mx} = \Delta M_x / h$, and converting it into the form of power, that is $P_{mx} = F_{mx}U_s$. Defining $\overline{P_{mx}}$ as the dimensionless coefficient of P_{mx}, the formulas are as follows:

$$C_E = \frac{P_b}{0.5\rho U_s^3 A} = \frac{0.5\rho_b V_b^3 A_b}{0.5\rho U_s^3 A} \tag{6}$$

$$\overline{P_{mx}} = \frac{P_{mx}}{0.5\rho U_s^3 A} \tag{7}$$

Where P_b stands for the power that is caused by blowing air at different speeds; $\rho_b = 1.225$ kg/m^3 represents the density of the blown air; A_b is the area of the air-blowing slots.

Then the mitigation efficiency of air-blowing on the rolling moment is defined as $C_E / \overline{P_{mx}}$, and $(1- C_E / \overline{P_{mx}}) \times 100\%$ is the energy utilization rate. When blowing air at a lower speed can achieve great M_x reduction, the $C_E / \overline{P_{mx}}$ value is small and the energy utilization rate is large, which means that low energy achieves a high mitigation effect. The energy utilization rates of the three cars obtained by blowing air at the speed of $0.05U_s$ - $0.3U_s$ are shown in Table 2.

Table 2. The energy utilization rates obtained by blowing air at the speed of $0.05U_s$ - $0.3U_s$

	The energy utilization rate					
	$0.05U$	$0.1U$	$0.15U$	$0.2U$	$0.25U$	$0.3U$
Head car	99.95%	99.67%	98.92%	97.64%	95.69%	92.80%
Middle car	99.91%	99.33%	97.83%	94.83%	92.40%	88.16%
Tail car	99.93%	99.37%	97.97%	95.32%	92.39%	86.80%

From the data in Table 2, it can be found that when blowing at a speed of $0.05U_s$, the energy utilization rate is close to 100%. On this basis, as V_b increases, the energy utilization rate gradually decreases, and the degree of reduction gradually increases. When blowing air at a speed of $0.3U_s$, the energy losses of the head, middle, and tail cars are 8.2%, 11.84%, and 13.2%, respectively. It can be seen that continuing to increase the blowing speed can further reduce the rolling moment of the train, but the degree of slowing down gradually weakens, which is also the reason why the maximum blowing speed of this paper is $0.3U_s$. However, a trade-off needs to be highlighted: when the risk of overturning is manageable, we should prioritize the economy of train operation, and consider using smaller blowing speeds to achieve higher energy utilization; when the crosswind is more severe, the safety of train becomes the primary concern, and we should then increase the allowable energy loss to achieve more overturning moment reduction and increase the safety threshold.

4. Conclusions

This paper used the IDDES method based on the SST k-ω turbulence model to explore the mitigating effect of air-blowing at the leeward side (*LWS*) of the train on the lateral aerodynamic forces of the train. The different air-blowing positions and different air-blowing speeds V_b were considered. The main conclusions are drawn below:

(1) The best mitigating effect was achieved when blowing air is applied at three cars simultaneously (HMT). The rolling moments of the three cars were reduced by 6.21%, 4.75%, and 19.67% respectively. The reduction rate of the rolling moment of the head car shows an increasing trend with the increase of air-blowing speed. When $V_b = 0.3U_s$, in the case of HTM, the rolling moments of the three cars were reduced by 7.71%, 7.25%, and 25.46% respectively. This proves that the air blowing strategy proposed in this study can improve the system dynamics performance of trains under cross wind and increase the operating safety threshold.

(2) The *LWS* flow field structure is composed of a vortex (V1), which is mainly influenced by air-blowing at the head car. After blowing air, one of the minus pressure

zones (*MPZ*) of the head car surface disappeared due to the position of vortex formation being delayed, the range and negative value of the other *MPZ* generally decreased with the increases of V_b. Blowing air at the middle car and the tail car has no obvious influence on V1, but changes the pressure of the surface around the air-blowing slots by interfering with the air that comes from the bottom of the train.

(3) The rolling moment of the train can be reduced by increasing the air-blowing speed, but the energy utilization rate of blowing air decreases with the increasing V_b. A trade-off needs to be considered between the overturning moment reduction and the energy utilization rate of air-blowing, which relates to the safety, economy, and sustainability of the train.

Acknowledgments

This work was supported by the National Natural Science Foundation of China (Grant No. 52202426), and a grant from the Research Grants Council (RGC) of the Hong Kong Special Administrative Region (SAR), China (Grants No. 15205723). The authors would also like to appreciate the funding support by the Innovation and Technology Commission of the Hong Kong SAR Government (Grant No. K-BBY1), and the Hong Kong and Macau Joint Research and Development Fund of Wuyi University (Grants No. 2019WGALH15, 2019WGALH17, 2021WGALH15), and the Guangdong Basic and Applied Basic Research Foundation of Department of Science and Technology of Guangdong Province (Grant No. 2021B1515130006), the Joint Fund of Guangdong Basic and Applied Basic Research Foundation - Youth Fund Project (Grant No. 2019A1515111052).

Reference

Asress, M.B., Svorcan, J., 2014. Numerical investigation on the aerodynamic characteristics of high-speed train under turbulent crosswind. Journal of Modern Transportation 22, 225-234. https://doi.org/10.1007/s40534-014-0058-7.

Avila-Sanchez, S., Pindado, S., Lopez-Garcia, O., Sanz-Andres, A., 2014. Wind tunnel analysis of the aerodynamic loads on rolling stock over railway embankments: The effect of shelter windbreaks. The Scientific World Journal 2014, https://doi.org/10.1155/2014/421829.

Baker, C., Cheli, F., Orellano, A., Paradot, N., Proppe, C., Rocchi, D., 2009. Cross-wind effects on road and rail vehicles. Vehicle system dynamics 47, 983-1022. https://doi.org/10.1080/00423110903078794.

Brambilla, E., Giappino, S., Tomasini, G., 2022. Wind tunnel tests on railway vehicles in the presence of windbreaks: Influence of flow and geometric parameters on aerodynamic coefficients. Journal of Wind Engineering Industrial Aerodynamics 220, 104838. https://doi.org/10.1016/j.jweia.2021.104838.

Che, Z.-X., Huang, S., Li, Z.-W., Chen, Z.-W., 2023. Aerodynamic drag reduction of high-speed maglev train based on air blowing/suction. Journal of Wind Engineering Industrial Aerodynamics 233, 105321.

https://doi.org/10.1016/j.jweia.2023.105321.
Chen, Z.-W., Guo, Z.-H., Ni, Y.-Q., Liu, T.-H., Zhang, J., 2023. A suction method to mitigate pressure waves induced by high-speed maglev trains passing through tunnels. Sustainable Cities Society 104682. https://doi.org/10.1016/j.scs.2023.104682.
Chen, Z.-W., Liu, T.-H., Yan, C.-G., Yu, M., Guo, Z.-J., Wang, T.-T., 2019. Numerical simulation and comparison of the slipstreams of trains with different nose lengths under crosswind. Journal of Wind Engineering Industrial Aerodynamics 190, 256-272. https://doi.org/10.1016/j.jweia.2019.05.005.
Chen, Z.-W., Ni, Y.-Q., Wang, Y.-W., Wang, S.-M., Liu, T.-H., 2022. Mitigating crosswind effect on high-speed trains by active blowing method: a comparative study. Engineering Applications of Computational Fluid Mechanics 16, 1064-1081. https://doi.org/10.1080/19942060.2022.2064921.
Chen, Z., Hashmi, S.A., Liu, T., Hemida, H., 2020a. Effect of a train's cross-sectional shapes on its aerodynamic performance subjected to crosswinds at a windbreak transition, 2020 World Congress on Advances in Civil, Environmental, & Materials Research (ACEM20).
Chen, Z., Liu, T., Jiang, Z., Guo, Z., Zhang, J., 2018. Comparative analysis of the effect of different nose lengths on train aerodynamic performance under crosswind. Journal of Fluids Structures 78, 69-85. https://doi.org/10.1016/j.jfluidstructs.2017.12.016.
Chen, Z., Liu, T., Yu, M., Chen, G., Chen, M., Guo, Z., 2020b. Experimental and numerical research on wind characteristics affected by actual mountain ridges and windbreaks: a case study of the Lanzhou-Xinjiang high-speed railway. Engineering Applications of Computational Fluid Mechanics 14, 1385-1403. https://doi.org/10.1080/19942060.2020.1831963.
Deng, E., Yue, H., Ni, Y.-Q., He, X.-H., Yang, W.-C., Chen, Z.-W., 2023a. Wake dynamic characteristics of windproof structures in embankment–bridge sections along a high-speed railway under natural strong crosswinds. Physics of Fluids 35, 055109. https://doi.org/10.1063/5.0147079.
Deng, E., Yue, H., Ni, Y.-Q., Wang, Y.-W., He, X.-H., Chen, Z.-W., 2023b. A turbulent crosswind simulation method at high-speed railway tunnel entrance: Based on field test and geometric turbulence generator. Physics of Fluids 35, https://doi.org/10.1063/5.0133292.
Gallagher, M., Morden, J., Baker, C., Soper, D., Quinn, A., Hemida, H., Sterling, M., 2018. Trains in crosswinds–comparison of full-scale on-train measurements, physical model tests and CFD calculations. Journal of Wind Engineering Industrial Aerodynamics 175, 428-444. https://doi.org/10.1016/j.jweia.2018.03.002.
Gao, H., Liu, T., Gu, H., Jiang, Z., Huo, X., Xia, Y., Chen, Z., 2021. Full-scale tests of unsteady aerodynamic loads and pressure distribution on fast trains in crosswinds. Measurement 186, 110152. https://doi.org/10.1016/j.measurement.2021.110152.
Guo, Z., Liu, T., Yu, M., Chen, Z., Li, W., Huo, X., Liu, H., 2019. Numerical study for the aerodynamic performance of double unit train under crosswind. Journal of Wind Engineering Industrial Aerodynamics 191, 203-214. https://doi.org/10.1016/j.jweia.2019.06.014.
Guo, Z., Liu, T., Liu, Z., Chen, X., Li, W., 2021. An IDDES study on a train suffering a crosswind with angles of attack on a bridge. Journal of Wind Engineering and Industrial Aerodynamics 217, 104735. https://doi.org/10.1016/j.jweia.2021.104735
Hashmi, S.A., Hemida, H., Soper, D., 2019. Wind tunnel testing on a train model subjected to crosswinds with different windbreak walls. Journal of Wind Engineering Industrial Aerodynamics 195, 104013. https://doi.org/10.1016/j.jweia.2019.104013.

Hemida, H., Krajnović, S., 2008. LES study of the influence of a train-nose shape on the flow structures under cross-wind conditions. Journal of Fluids Engineering 130, https://doi.org/10.1115/1.2953228.

Huang, S., Hemida, H., Yang, M., 2016. Numerical calculation of the slipstream generated by a CRH2 high-speed train. Proceedings of the Institution of Mechanical Engineers, Part F: Journal of Rail Rapid Transit 230, 103-116. https://doi.org/10.1177/0954409714528891.

Li, X., Zhou, D., Jia, L., Yang, M., 2018. Effects of yaw angle on the unsteady aerodynamic performance of the pantograph of a high-speed train under crosswind. Journal of Wind Engineering Industrial Aerodynamics 182, 49-60. https://doi.org/10.1016/j.jweia.2018.09.009.

Liu, D., Wang, T., Liang, X., Meng, S., Zhong, M., Lu, Z., 2020. High-speed train overturning safety under varying wind speed conditions. Journal of Wind Engineering Industrial Aerodynamics 198, 104111. https://doi.org/10.1016/j.jweia.2020.104111.

Liu, F., Zhou, W., Niu, J.-q., Zhang, J., 2019. Impact of increased linings on pressure transients induced by a train passing through a tunnel. Sustainable cities society 45, 314-323. https://doi.org/10.1016/j.scs.2018.10.030.

Liu, T., Chen, Z., Zhou, X., Zhang, J., 2018. A CFD analysis of the aerodynamics of a high-speed train passing through a windbreak transition under crosswind. Engineering Applications of Computational Fluid Mechanics 12, 137-151. https://doi.org/10.1080/19942060.2017.1360211.

Liu, T., Wang, L., Gao, H., Xia, Y., Guo, Z., Li, W., Liu, H., 2022. Research progress on train operation safety in xinjiang railway under wind environment. Transportation Safety and Environment 4, tdac005. https://doi.org/10.1093/tse/tdac005

Lou, P., Tao, W., Cai, C., He, X., Zou, Y., Ai, Y., 2022. Influence of Wind Barriers with Different Curvatures on Crosswind Aerodynamic Characteristics of a Train-Bridge System. Applied Sciences 12, 1747. https://doi.org/10.3390/app12031747.

Mohebbi, M., Rezvani, M., 2018a. The impact of air fences geometry on air flow around an ICE3 high speed train on a double line railway track with exposure to crosswinds. Journal of Applied Fluid Mechanics 11, 743-754. https://doi.org/10.29252/jafm.11.03.27862.

Mohebbi, M., Rezvani, M.A., 2018b. Multi objective optimization of aerodynamic design of high speed railway windbreaks using Lattice Boltzmann Method and wind tunnel test results. International Journal of Rail Transportation 6, 183-201. https://doi.org/10.1080/23248378.2018.1463873.

Mohebbi, M., Rezvani, M.A., 2018c. Two-dimensional analysis of the influence of windbreaks on airflow over a high-speed train under crosswind using lattice Boltzmann method. Proceedings of the Institution of Mechanical Engineers, Part F: Journal of RailRapid Transit 232, 863-872. https://doi.org/10.1177/0954409717699502.

Mohebbi, M., Rezvani, M.A., 2019. Analysis of the effects of lateral wind on a high speed train on a double routed railway track with porous shelters. Journal of Wind Engineering Industrial Aerodynamics 184, 116-127. https://doi.org/10.1016/j.jweia.2018.11.011.

Mohebbi, M., Rezvani, M.A., 2021. 2D and 3D numerical and experimental analyses of the aerodynamic effects of air fences on a high-speed train. Wind Structures 32, 539-550. https://doi.org/10.12989/was.2021.32.6.539.

Mohebbi, M., Safaee, A.M., 2022. The optimum model determination of porous barriers in high-speed tracks. Proceedings of the Institution of Mechanical Engineers, Part F: Journal of Rail Rapid Transit 236, 15-25. https://doi.org/10.1177/0954409721995323.

Muld, T.W., Efraimsson, G., Henningson, S, D., 2012. Flow structures around a high-speed train extracted using proper orthogonal decomposition and dynamic mode decomposition. Computers & Fluids 57, 87-97. https://doi.org/10.1016/j.compfluid.2011.12.012.

Muñoz-Paniagua, J., García, J., 2019. Aerodynamic surrogate-based optimization of the nose shape of a high-speed train for crosswind and passing-by scenarios. Journal of Wind Engineering Industrial Aerodynamics 184, 139-152. https://doi.org/10.1016/j.jweia.2018.11.014.

Niu, J., Liang, X., Zhou, D., 2016. Experimental study on the effect of Reynolds number on aerodynamic performance of high-speed train with and without yaw angle. Journal of Wind Engineering Industrial Aerodynamics 157, 36-46. https://doi.org/10.1016/j.jweia.2016.08.007.

Niu, J., Zhou, D., Liang, X., 2018. Numerical investigation of the aerodynamic characteristics of high-speed trains of different lengths under crosswind with or without windbreaks. Engineering Applications of Computational Fluid Mechanics 12, 195-215. https://doi.org/10.1080/19942060.2017.1390786.

Noguchi, Y., Suzuki, M., Baker, C., Nakade, K., 2019. Numerical and experimental study on the aerodynamic force coefficients of railway vehicles on an embankment in crosswind. Journal of Wind Engineering Industrial Aerodynamics 184, 90-105. https://doi.org/10.1016/j.jweia.2018.11.019.

Rezvani, M.A., Mohebbi, M., 2014. Numerical calculations of aerodynamic performance for ATM train at crosswind conditions. Wind Structures 18, 529-548. https://doi.org/10.12989/was.2014.18.5.529.

Rong, L., Zhiqiang, Y., Guang, C., 2021. High-speed Train Running Safety under Random Wind Effect. Journal of Engineering Science Technology Review 14, https://doi.org/10.25103/jestr.144.05.

Tardu, S.F., Doche, O.L., 2009. Active control of turbulent drag by a localized blowing dissymmetric in time. Experiments in Fluids 47, 19-26. https://doi.org/10.1007/s00348-009-0630-9.

Tomasini, G., Giappino, S., Cheli, F., Schito, P., 2016. Windbreaks for railway lines: Wind tunnel experimental tests. Proceedings of the Institution of Mechanical Engineers, Part F: Journal of Rail Rapid Transit 230, 1270-1282. https://doi.org/10.1177/0954409715596191.

Wahidi, R., Bridges, D.H., 2012. Effects of Distributed Suction on an Airfoil at Low Reynolds Number. Aiaa Journal 50, 523-539. https://doi.org/10.2514/1.J050913.

Wang, M., Wang, Z., Qiu, X., Li, X., Li, X., 2022. Windproof performance of wind barrier on the aerodynamic characteristics of high-speed train running on a simple supported bridge. Journal of Wind Engineering Industrial Aerodynamics 223, 104950. https://doi.org/10.1016/j.jweia.2022.104950.

Xia, Y., Liu, T., Su, X., Jiang, Z., Chen, Z., Guo, Z., 2022. Aerodynamic influences of typical windbreak wall types on a high-speed train under crosswinds. Journal of Wind Engineering Industrial Aerodynamics 231, 105203. https://doi.org/10.1016/j.jweia.2022.105203.

Xiang, H., Hu, H., Zhu, J., He, P., Li, Y., Han, B., 2022. Protective effect of railway bridge wind barriers on moving trains: An experimental study. Journal of Wind Engineering Industrial Aerodynamics 220, 104879. https://doi.org/10.1016/j.jweia.2021.104879.

Xiong, X., Zhu, L., Zhang, J., Li, A., Li, X., Tang, M.J.S.C., 2020. Field measurements of the interior and exterior aerodynamic pressure induced by a metro train passing through a tunnel. Sustainable Cities Society 53, 101928. https://doi.org/10.1016/j.scs.2019.101928.

Xu, K., Su, X., Bensow, R., Krajnovic, S., 2022. Drag reduction of ship airflow using steady Coanda effect. Ocean Engineering 266, 113051. https://doi.org/10.1016/j.oceaneng.2022.113051.

Xue, R.-D., Xiong, X.-H., Li, X.-B., Chen, G., 2023. Influence of turbulent incoming flow on aerodynamic behaviors of train at 90° yaw angle. Physics of Fluids 35, 015121. https://doi.org/10.1063/5.0135930.

Yang, W., Deng, E., Zhu, Z., Lei, M., Shi, C., He, H., 2020. Sudden variation effect of aerodynamic loads and safety analysis of running trains when entering tunnel under crosswind. Applied Sciences 10, 1445. https://doi.org/10.3390/app10041445.

Zhang, J., Gao, G., Liu, T., Li, Z., 2017a. Shape optimization of a kind of earth embankment type windbreak wall along the Lanzhou-Xinjiang railway. Journal of Applied Fluid Mechanics 10, 1189-1200. https://doi.org/10.18869/ACADPUB.JAFM.73.241.27353.

Zhang, L., Yang, M.-z., Liang, X.-f., 2018. Experimental study on the effect of wind angles on pressure distribution of train streamlined zone and train aerodynamic forces. Journal of Wind Engineering Industrial Aerodynamics 174, 330-343. https://doi.org/10.1016/j.jweia.2018.01.024.

Zhang, T., Guo, W.-w., Du, F., 2017b. Effect of windproof barrier on aerodynamic performance of vehicle-bridge system. Procedia engineering 199, 3083-3090. https://doi.org/10.1016/j.proeng.2017.09.426.

Zhou, L., Liu, T., Chen, Z., Li, W., Guo, Z., He, X., Wang, Y., 2021. Comparison study of the effect of bridge-tunnel transition on train aerodynamic performance with or without crosswind. Wind Structures 32, 597-612. https://doi.org/10.12989/was.2021.32.6.597.

Zou, S., He, X., Wang, H., 2020. Numerical investigation on the crosswind effects on a train running on a bridge. Engineering Applications of Computational Fluid Mechanics 14, 1458-1471. https://doi.org/10.1080/19942060.2020.1832920.